scientific reports

Check for updates

OPEN

Forming mechanism of equilibrium and non-equilibrium metallurgical phases in dissimilar aluminum/steel (Al–Fe) joints

Shun-Li Shang[1]✉, Hui Sun[1], Bo Pan[2], Yi Wang[1], Adam M. Krajewski[1], Mihaela Banu[3], Jingjing Li[2] & Zi-Kui Liu[1]

Forming metallurgical phases has a critical impact on the performance of dissimilar materials joints. Here, we shed light on the forming mechanism of equilibrium and non-equilibrium intermetallic compounds (IMCs) in dissimilar aluminum/steel joints with respect to processing history (e.g., the pressure and temperature profiles) and chemical composition, where the knowledge of free energy and atomic diffusion in the Al–Fe system was taken from first-principles phonon calculations and data available in the literature. We found that the metastable and ductile (judged by the presently predicted elastic constants) Al_6Fe is a pressure (*P*) favored IMC observed in processes involving high pressures. The $MoSi_2$-type Al_2Fe is brittle and a strong *P*-favored IMC observed at high pressures. The stable, brittle η-Al_5Fe_2 is the most observed IMC (followed by θ-$Al_{13}Fe_4$) in almost all processes, such as fusion/solid-state welding and additive manufacturing (AM), since η-Al_5Fe_2 is temperature-favored, possessing high thermodynamic driving force of formation and the fastest atomic diffusivity among all Al–Fe IMCs. Notably, the ductile $AlFe_3$, the less ductile AlFe, and most of the other IMCs can be formed during AM, making AM a superior process to achieve desired IMCs in dissimilar materials. In addition, the unknown configurations of Al_2Fe and Al_5Fe_2 were also examined by machine learning based datamining together with first-principles verifications and structure predictions. All the IMCs that are not *P*-favored can be identified using the conventional equilibrium phase diagram and the Scheil-Gulliver non-equilibrium simulations.

Joining of dissimilar materials has become increasingly important to create lightweight, high-performance, and economic structures employed in various industries, for example, automotive[1], aerospace[2,3], marine[4], and information technology[5]. Specially, joining of aluminum (Al) to steel/iron (Fe) is of eminent technical interest due to the potential use of two essential engineering materials in the same design[1,6]. It is known that mechanical properties of dissimilar materials are strongly affected by the type, amount/thickness, and morphology of metallurgical phases formed at the bonding interfaces. For example, the formation of brittle intermetallic compounds (IMCs), such as η-Al_5Fe_2[7,8], is usually detrimental to the performance of dissimilar materials joints owing to the reduction of materials' strength, ductility, and fracture toughness. A great deal of effort in chemistry and process design is hence required to avoid or reduce their formation in dissimilar materials, demanding fundamental understanding of phase stability of IMCs during various processes, for example, different pressure (*P*) and temperature (*T*) profiles under a given chemical composition.

Relevant to the present focus of Al–Fe joints, there are six IMCs shown in the equilibrium Al–Fe phase diagram under external pressure $P = 0$ GPa; see Fig. 1, which was modelled by the CALPHAD (calculations of phase diagram) approach by Sundman et al.[9]. It includes the stable IMCs of θ-$Al_{13}Fe_4$, η-Al_5Fe_2, Al_2Fe, AlFe (in B2 structure), $AlFe_3$ ($D0_3$), and the metastable ε-Al_8Fe_5 ($D8_2$). In addition, the other metastable IMCs include Al_6Fe and Al_mFe ($4 \le m \le 4.4$)[10], which are absent in Fig. 1. It is believed that the Al-rich IMCs ($Al_{13}Fe_4$, Al_5Fe_2, and Al_2Fe) are brittle and favor crack nucleation in the joints, while the Fe-rich IMCs (i.e., the BCC based AlFe and $AlFe_3$) show higher ductility and strength[7,8]. The ductility and brittleness of these IMCs are shown in Fig. 2

[1]Department of Materials Science and Engineering, Pennsylvania State University, University Park, PA 16802, USA. [2]Department of Industrial and Manufacturing Engineering, Pennsylvania State University, University Park, PA 16802, USA. [3]Department of Mechanical Engineering, University of Michigan, Ann Arbor, MI 48109, USA. ✉email: sus26@psu.edu

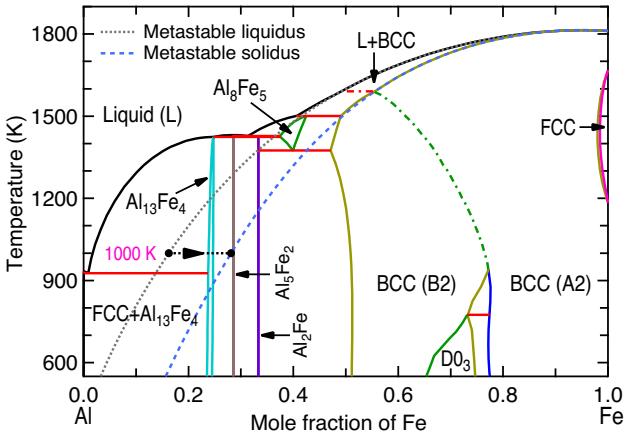

Figure 1. Calculated Al–Fe phase diagram based on CALPHAD modeling by Sundman et al.[9]. The metastable liquidus and solidus lines are plotted to analyze the formation of non-equilibrium phases from the supersaturated solution phase. One example at 1000 K is shown for phase equilibrium from the supercooled liquid with composition $x_{Fe} = 0.163$ to the supersaturated BCC phase with $x_{Fe} = 0.281$, then the composition 0.281 is used to calculate thermodynamic driving forces of IMCs at 1000 K; see Fig. 6.

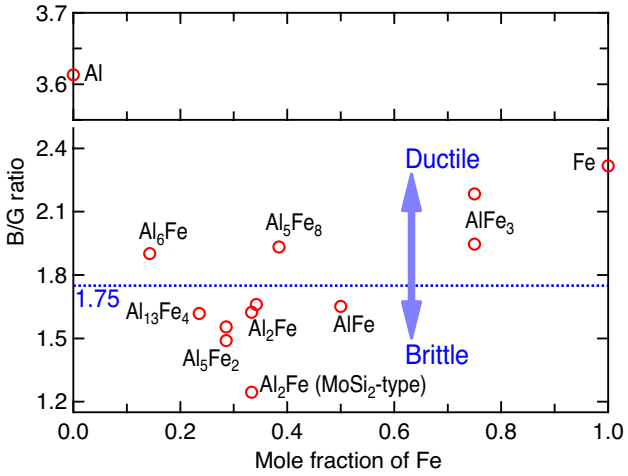

Figure 2. Calculated bulk modulus versus shear modulus (B/G) ratios of Al–Fe IMCs based on the present DFT calculations; see details in Table S3. Note that Pugh's criterion[11] of 1.75 is a rough value to separate the ductile and brittle materials, as discussed in the authors' responses to Reviewers in Ref. 12.

according to Pugh's criterion[11,12], i.e., the ratio of bulk modulus versus shear modulus (B/G) based on the present first-principles calculations (*cf.*, "Details of first-principles calculations" section). It indicates the ductile Al_6Fe, Al_5Fe_8, and $AlFe_3$; the less ductile $Al_{13}Fe_4$ and AlFe; and the brittle Al_5Fe_2 and Al_2Fe. Table 1 summarizes the Al–Fe IMCs formed in different processes reported in the literature. The metastable, ductile Al_6Fe was observed in the processes of direct chill casting (example #1 in Table 1)[10], high-pressure die casting (#2)[13], equal channel angular extrusion (#3)[14], tungsten inert gas (TIG) welding-brazing (#4)[15], and additive manufacturing (AM) via laser powder bed fusion (#5)[16]. These observations suggest that Al_6Fe is an IMC existing at high pressures. Table 1 further depicts that most of the stable and even metastable Al–Fe IMCs were observed in AM processes. For example, Al_6Fe, $Al_{13}Fe_4$, Al_2Fe, Al_5Fe_2, AlFe, and/or $AlFe_3$ were formed during the processes of laser powder bed fusion[16], laser cladding[17], direct energy deposition[18], laser metal deposition[19], and/or wire-arc AM[20,21] (see examples #5 to #10 in Table 1). In particular, the ductile (or less brittle) $Al_{13}Fe_4$, AlFe, and $AlFe_3$[20–22] (examples #9 to #11) were observed in Al–Fe based functional graded materials fabricated by additive manufacturing. These experiments indicate that AM is an exceptional process to tailor compositions and in turn the desired IMCs. Note that the AM induced residual stress is usually less than 1 GPa, for example, 290–416 MPa in 304L stainless steel[23], and up to ~ 660 and 200 MPa for tensile and compressive, respectively, in 316L stainless steel[24]. These stresses are usually negligibly small to induce solid state phase transition. In the fusion and/or solid-state welding joints, Al_5Fe_2 is the most observed IMC (usually adjacent to iron/steel) followed by $Al_{13}Fe_4$ (usually adjacent to Al) processed by, for example, laser welding[25–27] (see examples #13 to #15 in Table 1), friction-type

#, Ref	Materials	Methods	Observed Al–Fe IMCs
1[10]	Sheet ingots of Al alloys: 1050, − 1100, and − 5005	Direct-chill casting	$Al_{13}Fe_4$ with cooling rate < 3 K/s; Al_6Fe with cooling rate from 1–3 to 10–20 K/s; and Al_mFe ($4 \le m \le 4.4$) with cooling rate > 20 K/s
2[13]	Al-5Mg-*x*Fe-0.6Mn ($x = 0.1–2$ wt.%)	High pressure die casting at 720 °C	$Al_6(Fe,Mn)$ and $Al_{13}(Fe,Mn)_4$[a]
3[14]	Al-3Fe alloy	Equal channel angular extrusion at room temperature	Al_6Fe
4[15]	Al alloy 5A06 and SUS321 steel sheets	Tungsten inert gas welding-brazing with Al filler	Al_6Fe in welded seam with Nocolok flux; and $Al_{13}Fe_4$ in the IMC layer
5[16]	Al-2.5wt.% Fe alloy powders	Laser powder bed fusion (LPBF)	$Al_{13}Fe_4$ (reduced in the LPBF samples compared to ingots) and Al_6Fe
6[17]	Al and Fe powders	Layer by layer laser cladding	Al_2Fe (with 34–52 at. % Al cases); and Al_5Fe_2 and $Al_{13}Fe_4$ (with > 52 at. % Al cases)
7[18]	Al and Fe powders	Direct energy deposition (DED) type process	$AlFe_3$ (for composition Fe-28Al); $AlFe_3$ + AlFe (for Fe-36Al); and AlFe (for Fe-50Al)
8[19]	Fe-28Al and Al powders	Laser metal deposition for graded Fe-Al/steel samples and heat treated at 700 °C	AlFe and Al_2Fe (cracks originated in Al-rich part) followed by Al-rich AlFe below
9[20]	Al and Fe wires	Wire-arc AM (WAAM) for Fe-AlFe functionally graded material (FGM)	$AlFe_3$ and AlFe
10[21]	Al and Fe wires	WAAM to fabricate Fe-rich IMC (25 at.% Al)	$AlFe_3$
11[22]	Pure Al with Al-10 wt.% Fe	Vacuum centrifugal method to make Al-$Al_{13}Fe_4$ FGM	$Al_{13}Fe_4$
12[45]	Compressed mixture of Al and Fe powders	High-temperature reactive sintering (800 and 900 °C)	Al_5Fe_2 and Al_2Fe; and AlFe (long-term annealing)
13[25]	Al-steel overlap joints	Laser welding (up to 1200 °C)	Al_5Fe_2 (assuming diffusion from Fe to Al only)
14[26]	Al alloy 6061-T6 and galvanized steel DP590	Laser welding without filler	$Al_{13}Fe_4$ and Al_5Fe_2 with linear energy density of 162 J/mm; $Al_{13}Fe_4$, Al_5Fe_2, and AlFe with 309 J/mm
15[27]	Al alloy 5083 and low alloy steel (XF350) plates	Fiber laser welding with 8 kW of max power	Al_5Fe_2 near steel (main) and $Al_{13}Fe_4$ near Al
16[28]	Pure Al (1100) and low carbon steel	Friction stir welding	Al_5Fe_2 and $Al_{13}Fe_4$
17[29]	Al alloy (5186) and low carbon steel	Friction stir welding	Al_5Fe_2 (adjacent to Fe) and $Al_{13}Fe_4$ (adjacent to Al, facilitated by Fe diffusion)
18[30]	Al sheet (6061) and galvannealed steel sheet	Friction stir welding	$Al_{13}Fe_4$ (large size, diffusion induced) and $AlFe_3$ (small size)
19[31]	Al alloy 5754 with coated DP600 or 22MnB5 steel	Diffusion bonding by friction stir welding	Al_5Fe_2 in low welding speeds (16 mm/min) and AlFe in 45 mm/min
20[32]	Al alloy 5083 and steel (< 0.1 wt.% C) sheets	Annealing of friction stir lap welds	Al_5Fe_2 (major) and $Al_{13}Fe_4$ annealed at 673 K for 180 min
21[33]	Al alloy 6061-T6 and AISI 1018 steel	Friction welding	Al_5Fe_2 and AlFe (suggested based on compositions)
22[34]	Al sheet (6016) and galvanized IF-steel sheet	Friction stir spot welding	$Al_{13}Fe_4$, Al_5Fe_2, and Al_2Fe
23[35]	Al alloy (surfalex 6 s) and ultrahigh strength steel	Friction stir scribe welding	Al_5Fe_2 (in the middle) or $Al_{13}Fe_4$ with Fe/Al solid solution depending on the weld regions
24[36]	Al alloy (1050) sheets and Fe particles	Friction stir processing	Al_5Fe_2 close to Fe particle; and $Al_{13}Fe_4$ close to Al matrix
25[37]	Al sheet (6061 T4) and coated steel sheet	Cold metal transfer fusion welding	$Al_{13}Fe_4$ (at the interface to Al) and Al_5Fe_2 (tongue-like, extended into steel)
26[38]	Al alloy wire (ER5356) and Zn-coated steel	Double electrode gas metal arc welding	Al_5Fe_2 (major) and $Al_{13}Fe_4$
27[39]	Pure Al and Fe	Solid Fe in liquid Al at 850 °C for 0.6 h	Al_5Fe_2 layer with needle-like or flake $Al_{13}Fe_4$
28[40]	Pure Al and Fe	Immersion testing of solid Fe and liquid Al (700–900 °C)	Al_5Fe_2 (adjacent to Fe) and $Al_{13}Fe_4$ (adjacent to Al)
29[41]	Pure Al and Fe	Immersion testing of solid Fe and liquid Al (700–900 °C)	Al_5Fe_2 and $Al_{13}Fe_4$
30[42]	Pure Al plate and pure Fe sheet	Diffusion couples	Al_5Fe_2 (at 873 K for 9 h) and $Al_{13}Fe_4$ (at 913 K for 528 h)
31[43]	Pure Al and Fe rods (diffusion couples)	Al and Fe by isothermal bonding and then annealed at 973–1073 K	Al_5Fe_2 (major, tongue-like) close to Fe and $Al_{13}Fe_4$ close to Al
32[44]	Al–Fe diffusion couples	Riveting Al rod into Fe plate	$Al_{13}Fe_4$ formed in Fe side at 600 °C (Al diffuses to Fe) and Al_5Fe_2 formed in both Al and Fe sides > 700 °C (due to Fe and Al interdiffusion)
33[46]	Hot-dip Al-coated steel	Aluminized steel at 800 °C for 60 s, then 680 °C for 60 s	$Al_{13}Fe_4$ just beneath Al cover layer and Al_5Fe_2 just underneath steel

Table 1. Experimentally observed Al–Fe IMCs in various processes in the literature. Note that the compositions quoted in this table are in wt.% unless otherwise stated. [a]Addition of Mn promotes the formation of $Al_6(Fe,Mn)$.

solid state welding[28–36] (#16 to #24), cold metal transfer fusion welding[37] (#25), and double electrode gas metal arc welding[38] (#26). The other IMCs such as Al_2Fe and $AlFe_3$ were also observed in welding processes, depending on welding conditions (e.g., energy inputs)[7]; see examples #14, #21, and #22 in Table 1. The same as those in welding processes, Al_5Fe_2 (majorly) and $Al_{13}Fe_4$ were also observed in immersion testing with solid Fe and liquid Al[39–41] (see examples #27 to #29 in Table 1), Al–Fe diffusion couples[42–44] (#30 to #32), high-temperature reactive sintering[45] (#12), and aluminized steel[46] (#33).

Despite considerable observations as shown in Table 1, the underlying mechanism regarding the formation of Al–Fe IMCs is still lacking, albeit phase stability is known to be regulated by processing history involving *T* and *P* profiles for a given chemistry[47]. The phase diagram, as a foundational guide for any work in materials

science and engineering[48], is the most used tool to analyze equilibrium IMCs under a given temperature and composition (usually under external pressure $P = 0$ GPa). Additionally, non-equilibrium simulations in terms of the Scheil-Gulliver model[49,50] can be used to analyze the forming IMCs in fast cooling processes by assuming that no diffusion takes place in the solid and that solute redistribution in the liquid is infinitely fast[51–53]. The Scheil simulations have been used, for example, to predict the formed IMCs in additively manufactured functionally graded metals[51,52] and to predict the temperatures of liquidus and solidus in steel[53]. In addition to the phase diagram, non-equilibrium IMCs can be predicted by calculating thermodynamic driving forces for the phases of interest with respect to supercooled liquid and associated solid phases; see the predicted interface phases at the Cu/solder joints by Lee et al.[54]. Also based on thermodynamics, non-equilibrium IMCs can be tailored by partitionless solidification or by chemical partition solidification with limited atomic diffusions; for example, the non-equilibrium solidification predicted in the Al-Sm system by Zhou and Napolitano[55]. It should be remarked that thermodynamic knowledge in the literature is usually at the ambient pressure or external pressure $P = 0$ GPa, thus hindering the analysis of P-favored phases such as Al_6Fe in the present work. In addition to thermodynamics, kinetics (diffusion) is another factor to regulate nucleation, growth, and coarsening of IMCs[56,57]. For example, Al_5Fe_2 and $Al_{13}Fe_4$ were formed due mainly to Al and/or Fe interdiffusion in some processes; see the examples #13, #17, #18, #30, #31, and #32 in Table 1.

The present work aims to unveil the forming mechanism of equilibrium and non-equilibrium IMCs in dissimilar aluminum to steel joints based on thermodynamic knowledge in the Al–Fe system from (1) the present first-principles and phonon calculations based on density functional theory (DFT) and (2) the CALPHAD modeling by Sundman et al.[9] and also based on kinetic (diffusion) knowledge reported in the literature[42,58,59]. Special attention in the present DFT calculations is paid to the P-included Gibbs energy in addition to the variable of temperature. The challenge for the present DFT calculations is the unknown atomic configurations of (i) Al_5Fe_2 caused by the partially occupied Wyckoff sites 4b and 8f. of space group $Cmcm$[60] and (ii) Al_2Fe caused by the disordered Al and Fe in one of the Wyckoff sites 2i of space group $P\bar{1}$[61]. To address this challenge, we adopt the following three approaches: (1) DFT-based USPEX (Universal Structure Predictor: Evolutionary Xtallography) predictions[62], (2) DFT-based examinations of all possible configurations for a given supercell, and (3) datamining by examining all possible configurations in the literature with their formation energies predicted by machine learning. In addition to the conventional equilibrium phase diagram, non-equilibrium Scheil simulations were also used to analyze the formation of Al–Fe IMCs. The present work indicates that the forming mechanism of IMCs in dissimilar Al–Fe joints (see examples in Table 1) can be explained well using phase diagram, Scheil simulations, thermodynamic driving forces, P- and T-included Gibbs energies, and atomic diffusion coefficients in the Al–Fe system.

Methodology

Atomic configurations of Al–Fe IMCs. Most of the Al–Fe IMCs together with the constituent elements of FCC Al and BCC Fe are ordered structures. Their structures can be found, for example, in the Materials Project (MP) database[63] or the Open Quantum Materials Database (OQMD)[64]; see the Supplementary Table S1. However, Al_5Fe_2 is an IMC with vacancies (Va) in its Wyckoff sites for Al atoms[60]. The structure of Al_5Fe_2 can be described by the following sublattice model according to its Wyckoff sites 4c, 8 g, 4b (occupation of 0.32 by Al), and 8f. (occupation of 0.24 by Al) of space group $Cmcm$[60], respectively,

$$(\mathrm{Fe})_4^c(\mathrm{Al})_8^g(\mathrm{Al},\mathrm{Va})_4^b(\mathrm{Al},\mathrm{Va})_8^f \tag{1}$$

For another IMC of Al_2Fe, Chumak et al.[61] indicated that it belongs to space group $P\bar{1}$ with one of its Wyckoff sites 2i mixed with Fe (occupation of 0.705) and Al (occupation of 0.295),

$$(\mathrm{Fe})_{10}(\mathrm{Al})_{24}(\mathrm{Al},\mathrm{Fe})_4^i \tag{2}$$

Atomic configurations of Al_5Fe_2 were determined as follows in the present work. First, all the independent Al_5Fe_2 configurations were generated by the ATAT code[65] using a 24-atom supercell, see Eq. (1). Second, we performed DFT calculations for the 14- to 16-atom configurations with one or two Al atoms in the Wyckoff sites 4b and 8f., respectively. For the composition of Al_5Fe_2, we also used the universal structure predictor—USPEX[62,66]—to predict the lowest energy configuration in terms of a 14-atom supercell; where the computational engine of USPEX is DFT-based calculations ("Details of first-principles calculations" section). In addition, we also examined the low energy configurations of Al_5Fe_2 suggested by Vinokur et al.[67].

Atomic configurations of Al_2Fe were also examined by the ATAT code[65] based on the mixing of Al and Fe in Wyckoff site 2i (see Eq. 2) by using both the 38- and 57-atom supercells of Al_2Fe. In addition, the $MoSi_2$-type configuration suggested by Tobita et al.[68] was included in the present work. Aiming to search for the possible configurations of Al_2Fe, we also adopted a datamining approach by considering all the AB_2-type configurations (~ 1.3 million) in the Materials Project (MP) database[63], the Open Quantum Materials Database (OQMD)[64], the Crystallography Open Database (COD)[69,70], and the Joint Automated Repository for Various Integrated Simulations (JARVIS) database[71]. The enthalpies of formation (ΔH_0) of these AB_2-type configurations were predicted by machine learning (ML) in terms of the tool of SIPFENN (structure-informed prediction of formation energy using neural networks)[72]. Here, SIPFENN requires only atomic configurations and atomic species, which allows efficient integration into datamining study within minutes. On a random 5% subset in the OQMD structures, SIPFENN could achieve a mean absolute error of 28 meV/atom (2.7 kJ/mol-atom) to predict ΔH_0[72]. For the SIPFENN suggested A_2B-type configurations with lower ΔH_0 values (more than 500 configurations were selected by considering the SIPFENN error bar up to 28 meV/atom), we performed DFT-based verifications. Notably, the present datamining approach found that the lowest energy configuration of Al_2Fe is also the $MoSi_2$-type.

First-principles thermodynamics. Thermodynamic properties at finite temperatures can be predicted by the DFT-based quasiharmonic approach, i.e., Helmholtz energy F for a given phase as a function of volume V and temperature T is determined by[73,74],

$$F(V,T) = E(V) + E_{vib}(V,T) + E_{el}(V,T) - T\left[S_{vib}(V,T) + S_{el}(V,T) + S_{conf}\right] \tag{3}$$

Correspondingly, the Gibbs energy can be evaluated by $G(P,T) = F(V,T)\,|_{P=fix} + PV$ at the given pressure of interest. Here, $E_{vib}(V,T)$ and $S_{vib}(V,T)$ are vibrational contributions (internal energy and entropy, respectively) determined by phonon densities of states (DOS's, about 6 volumes were calculated for each phase)[73,75]. $E_{el}(V,T)$ and $S_{el}(V,T)$ are thermal electronic contributions (internal energy and entropy, respectively) determined by electronic DOS's[73,75]. S_{conf} is ideal configurational entropy introduced to account for the IMCs with partially occupied Wyckoff sites, i.e., Al_5Fe_2 (described by Eq. 1) and Al_2Fe (Eq. 2),

$$S_{conf}^{Al_5Fe_2} = -\frac{4R\left(y_{Al}^{b}\log\left(y_{Al}^{b}\right) + y_{Va}^{b}\log\left(y_{Va}^{b}\right)\right)}{24} - \frac{8R\left(y_{Al}^{f}\log\left(y_{Al}^{f}\right) + y_{Va}^{f}\log\left(y_{Va}^{f}\right)\right)}{24} \tag{4}$$

$$S_{conf}^{Al_2Fe} = -\frac{4R\left(y_{Al}^{i}\log\left(y_{Al}^{i}\right) + y_{Fe}^{i}\log\left(y_{Fe}^{i}\right)\right)}{38} \tag{5}$$

where R is the gas constant and y the site fraction with the superscript being Wyckoff site (i.e., also the sublattice). Based on experimental measurements for Al_5Fe_2[60], $y_{Al}^{b} = 0.32$ ($y_{Al}^{f} = 0.24$) and $y_{Va}^{b} = 0.68$ ($y_{Va}^{f} = 0.76$) for Al and Va, respectively. Correspondingly, $y_{Al}^{i} = 0.295$ and $y_{Fe}^{i} = 0.705$ based on experiments for Al_2Fe[61].

$E(V)$ in Eq. (3) is the static energy at 0 K without the zero-point vibrational energy, which was determined by fitting the DFT calculated energy-volume (E-V) data points using a four-parameter Birch-Murnaghan equation of state (EOS)[73],

$$E(V) = k_1 + k_2 V^{-2/3} + k_3 V^{-4/3} + k_4 V^{-2} \tag{6}$$

where k_1, k_2, k_3, and k_4 are fitting parameters. Equilibrium properties for each phase (configuration) from this EOS include the equilibrium energy E_0, volume V_0, bulk modulus B_0, and the pressure derivative of bulk modulus B'. Usually, eight reliable data points were used for each EOS fitting in the present work.

It is worth mentioning that we ignored the contribution of anharmonicity to first-principles thermodynamics in Eq. (3), which can be accounted for by using such as molecular dynamics simulations[76,77]. In the present work, the relative Gibbs energy with respect to reference states (e.g., Al and Fe) was adopted to study phase stability, making the contribution of anharmonicity cancelled to some extent. In addition, we were trying to search for the possible "low energy atomic configurations" of Al_5Fe_2 and Al_2Fe (*cf.*, "Atomic configurations of Al–Fe IMCs" section), and we used the ideal configurational entropy in first-principles thermodynamics for the sake of simplicity (*cf.*, Eq. 3) for both Al_5Fe_2 and Al_2Fe, although the actual configurational entropy should be considered in terms of statistical mechanics (i.e., the partition function) by including all ergodic microstates (configurations) for a system (phase) of interest[78,79]. Note that even using the lowest energy atomic configurations of Al_5Fe_2 and Al_2Fe, we still need to consider configurational entropy due to the partially occupied Wyckoff sites. In summary, the sources of error in the present first-principles thermodynamics (Eq. 3) include the ignorance of anharmonicity, the adoption of ideal configurational entropy, the unknown atomic configurations of Al_5Fe_2 and Al_2Fe, and the approximations used in density functional theory such as the exchange–correlation (X-C) functional[80]. Nevertheless, the DFT-based quasiharmonic approach is still a predictive tool with great success to study thermodynamics in solid phases, see the examples in our review article[47].

Details of first-principles calculations. All DFT-based first-principles calculations in the present work were performed by the Vienna Ab initio Simulation Package (VASP)[81] with the ion–electron interaction described by the projector augmented wave method[82] and the X-C functional described by the generalized gradient approximation (GGA) developed by Perdew, Burke, and Ernzerhof (PBE)[83]. The same as those in the Materials Project[63], three electrons ($3s^2 3p^1$) were treated as valence electrons for Al and fourteen ($3p^6 3d^7 4s^1$) for Fe. In the VASP calculations, a plane wave cutoff energy of 293.2 eV was employed for structural relaxations and phonon calculations in terms of the Methfessel-Paxton method[84]. Final calculations of total energies and electronic DOS's were performed by the tetrahedron method with a Blöchl correction[85] using a wave cutoff energy of 520 eV. The employed k-points meshes for each structure are listed in the Supplementary Table S1. The self-consistency of total energy was converged to at least 10^{-6} eV/atom. Due to the magnetic nature of Fe, all Fe-containing materials were performed by the spin polarization calculations.

Phonon calculations were performed for each structure using the supercell approach[86] in terms of the YPHON code[87]. Here, the VASP code was again the computational engine in calculating force constants using the finite differences method. The employed supercell for each structure and the corresponding k-point meshes are given in the Supplementary Table S1. In addition, the single crystal elastic constants C_{ij}'s in the Al–Fe system were determined by applying the stress–strain method with the non-zero strains being ± 0.01; see details in[88,89]. The aggregate polycrystal properties were determined by using the Hill (H) approach[90,91] based on the predicted C_{ij} values, including bulk modulus (B_H), shear modulus (G_H), B_H/G_H ratio, Poisson's ratio (ν_H), and the anisotropy index A^U[92]. Note that the suggested DFT settings by USPEX[62,66] were used in the present work, aiming to search for the low energy configurations of Al_5Fe_2 by USPEX.

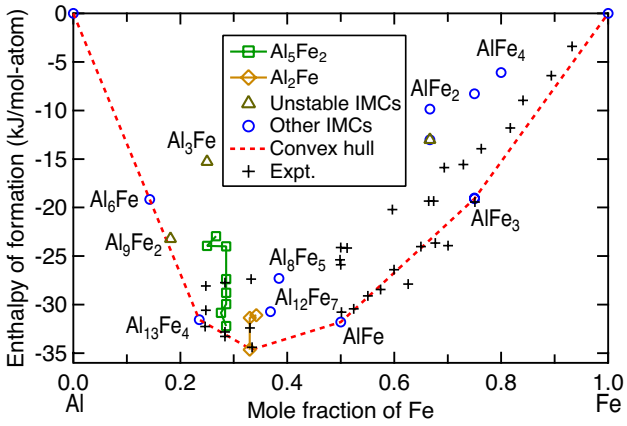

Figure 3. Predicted enthalpies of formation (ΔH_0) at $T=0$ K and $P=0$ GPa for Al–Fe IMCs by the present DFT calculations (see structural details and ΔH_0 values in Table S1). Note that the convex hull was plotted using the DFT results, the unstable IMCs were judged by imaginary phonon modes, and the experimental data (Expt.) were collected by Sundman et al.[9].

Formation of non-equilibrium IMCs through thermodynamic analysis. The decrease in Gibbs energy, $-\Delta G_m^{\alpha}$, for the precipitation of a new phase α (e.g., IMC) from a supersaturated solution (e.g., the supercooled liquid), is the thermodynamic driving force of formation, D, of the new α phase, i.e., $D=-\Delta G_m^{\alpha}$[93]. The IMC with the highest thermodynamic driving force of formation can be selected as the IMC that would form first, making the driving force D a reasonable criterion to predict the first-forming IMC[54]. Similarly to the analysis of interface phases formed at the Cu/solder joints by Lee et al.[54], for example, Fig. 1 shows that at 1000 K of the Al–Fe system, the supercooled liquid has a composition $x_{Fe}=0.163$ (mole fraction of Fe in the metastable liquidus), which is in equilibrium with the supersaturated BCC phase (i.e., the metastable solidus) with $x_{Fe}=0.281$. At this composition ($x_{Fe}=0.281$), we can calculate thermodynamic driving forces of the IMCs (such as $Al_{13}Fe_4$, Al_5Fe_2, Al_2Fe, and Al_8Fe_5) formed from the supersaturated BCC phase — the higher the driving force, the larger the possibility to form this IMC. In the present work, thermodynamic driving forces to form IMCs from the supersaturated BCC phase were calculated as a function of temperature using the modeled Al–Fe system by Sundman et al.[9] and the Thermo-Calc software[57].

In addition to thermodynamic driving forces, we can also use the non-equilibrium phase diagram, predicted by the Scheil-Gulliver simulations[49,50] (see its definition in the Introduction section), to predict the formation of IMCs in fast cooling processes, such as the AM process[51,52]. Here, we used the PyCalphad software[52,94] to calculate the Scheil non-equilibrium phase diagram with the Al–Fe thermodynamic description modelled by Sundman et al.[9].

Results and discussion

DFT-based phase stability of Al–Fe IMCs. In this section, we show first the phase stability of Al–Fe IMCs at temperature $T=0$ K and pressure $P=0$ GPa ("DFT-based phase stability of IMCs at T = 0 K and P = 0 GPa") aiming to demonstrate the capable of DFT-based calculations; and then, we show the phase stability of Al–Fe IMCs at finite temperatures and finite pressures ("DFT-based phase stability of IMCs at finite temperatures and finite pressures" section) through both the case studies of three reactions and the predicted P–T phase diagram.

DFT-based phase stability of IMCs at T = 0 K and P = 0 GPa. Figure 3 shows the predicted values of enthalpy of formation (ΔH_0) for Al–Fe IMCs based on the present DFT calculations at $T=0$ K and $P=0$ GPa. Detailed atomic configuration and ΔH_0 value of each IMC are given in the Supplementary Table S1; in particular, the predicted 14-atom configuration of Al_5Fe_2 by USPEX[62,66] is listed in the Supplementary Table S2. Figure 3 shows also the convex hull by DFT calculations to display the stable IMCs, the experimental ΔH_0 values collected by Sundman et al.[9] to measure the quality of the present DFT calculations, and the unstable configurations judged by imaginary phonon modes (not shown). It can be seen that (i) the DFT-predicted ΔH_0 values agree well with the experimental data which are scattered; (ii) Al_6Fe is close to but above the convex hull, indicating that it is metastable at $T=0$ K and $P=0$ GPa, and more attentions need to be paid to its phase stability at high temperatures and high pressures; (iii) Al_9Fe_2 is an unstable structure due to the existence of imaginary phonon modes and hence ignored in the present work; (iv) Al_5Fe_2 is a metastable phase at $T=0$ K and $P=0$ GPa, although various configurations have been examined in the present work (see the green open squares as well as the details in Table S1); (v) the $MoSi_2$-type Al_2Fe possesses the lowest energy and on the convex hull at $T=0$ K and $P=0$ GPa, but this configuration doesn't belong to space group $P\bar{1}$ as suggested by Chumak et al.[61]; and (vi) the IMCs of $Al_{13}Fe_4$, AlFe, and $AlFe_3$ are stable based on the convex hull. Figure 3 implies that, at the conditions of $T=0$ K and $P=0$ GPa, the DFT predicted ΔH_0 values for Al_5Fe_2 and non-$MoSi_2$-type Al_2Fe (i.e., the triclinic Al_2Fe[61]) are close to but above the convex hull, indicating that (a) the supercells used in the present work may be too small to

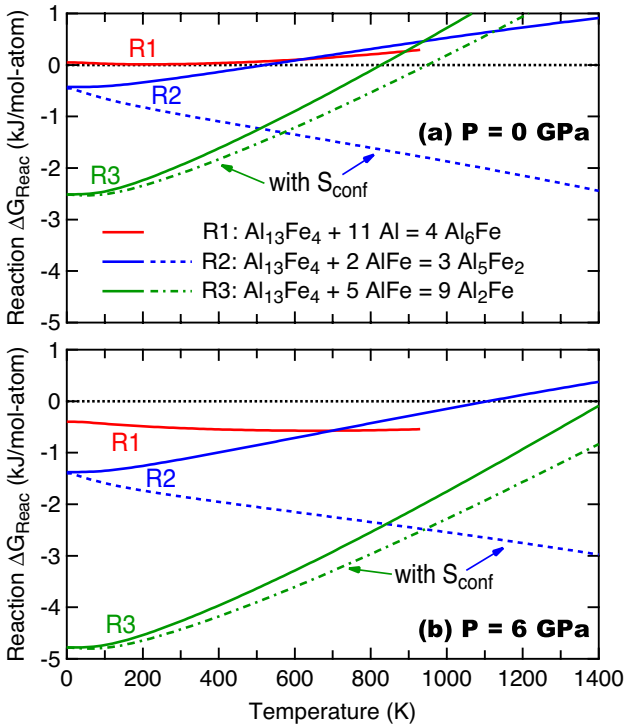

Figure 4. Reaction Gibbs energies (ΔG_{reac}'s) under external pressure $P = 0$ GPa (**a**) and 6 GPa (**b**) with and without considering the ideal configurational entropies (S_{conf}'s) of Al_5Fe_2 and Al_2Fe, respectively; see Eqs. (4) and (5). The ΔG_{reac} curves for reaction R1 are plotted up to 930 K, which is slightly below the melting point of Al (933 K).

search for the lowest energy atomic configurations, and (b) additional effects on phase stability such as temperature, pressure, and new approaches need to be considered. To this end as well as the suggestions by Fig. 3, phase stabilities of Al_6Fe, Al_5Fe_2, and Al_2Fe are further examined at finite temperatures and finite pressures (see Fig. 4).

DFT-based phase stability of IMCs at finite temperatures and finite pressures. Phase diagram at a given temperature and pressure can be constructed using the convex hull approach, i.e., by examining all reaction Gibbs energies, ΔG_{reac}, for a system of interest. Note that in general one reaction cannot determine phase stability in the whole temperature and pressure ranges. As test cases, Fig. 4 shows only the changes of ΔG_{reac} as a function of temperature and pressure ($P = 0$ and 6 GPa as two examples) for the following three reactions, aiming to understand phase stability of Al_6Fe as well as Al_5Fe_2 and Al_2Fe with respect to the given reference phases (instead of building the convex hull),

$$\mathrm{R1}: \ \mathrm{Al_{13}Fe_4} + 11\mathrm{Al} = 4\mathrm{Al_6Fe} \tag{7}$$

$$\mathrm{R2}: \ \mathrm{Al_{13}Fe_4} + 2\mathrm{AlFe} = 3\mathrm{Al_5Fe_2} \tag{8}$$

$$\mathrm{R3}: \ \mathrm{Al_{13}Fe_4} + 5\mathrm{AlFe} = 9\mathrm{Al_2Fe} \tag{9}$$

Here we choose the stable phases of Al, $Al_{13}Fe_4$, and AlFe (the B2 structure) as the reference states to examine phase stability of Al_6Fe, Al_5Fe_2 (using the configuration predicted by USPEX), and Al_2Fe (using the $MoSi_2$-type configuration predicted by SIPFENN). As mentioned at the end of "First-principles thermodynamics" section, the ideal configurational entropies together with the possible "low energy configurations" were used for Al_5Fe_2 and Al_2Fe, resulting in a large contribution of configurational entropy than the actual case. However, the predicted configurations of Al_5Fe_2 and Al_2Fe are still not the lowest energy ones based on the present approach, making the error by using the larger ideal configurational entropy cancelled to some extent. Also the ΔG_{reac} values with and without the contributions of ideal configurational entropy form an uncertainty range to analyze phase stability of Al–Fe IMCs.

Figure 4 shows that Al_6Fe is a T-unfavored (see R1) but a P-favored phase, which can be understood through phonon density of states as detailed in Supplementary Materials. Figure 4b. It shows that with increasing pressure (even less than 1 GPa) instead of increasing temperature, Al_6Fe becomes stable with respect to Al and $Al_{13}Fe_4$ (*cf.*, the reaction R1). Based on experimental observations such as the examples #1 to #5 in Table 1, Al_6Fe was formed in the processes associated with pressures (such as die casting and equal channel angular extrusion) and in high Al-containing samples (e.g., $x_{Al} > 0.9$). The reaction R2 (see Eq. 8) in Fig. 4a and b shows that Al_5Fe_2 is a

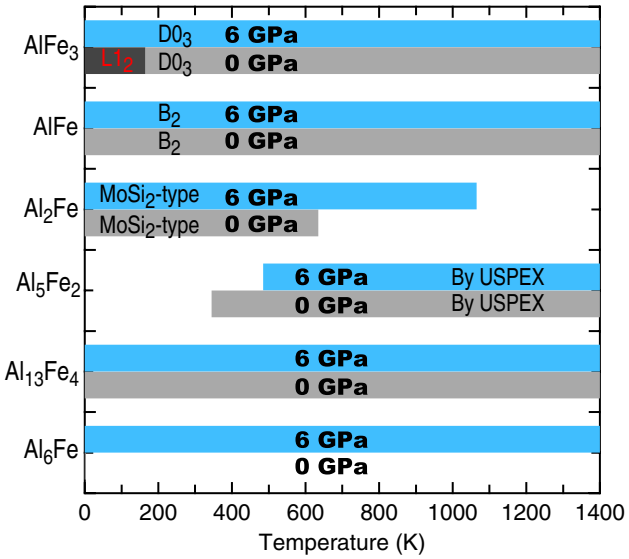

Figure 5. Phase stability (on the convex hull) of Al–Fe IMCs under external pressures of 0 and 6 GPa as a function of temperature (shown in the shaded regions) based on the present DFT calculations using Eq. (3). The predicted $L1_2$-$AlFe_3$ presented at low temperatures is due to the employed X-C functional of GGA, see discussion in main text.

T-unfavored but *P*-favored phase by ignoring the contribution of configurational entropy S_{conf}; see Eqs. 3 and 4. With S_{conf} contribution to ΔG_{reac}, Al_5Fe_2 becomes both the *T*- and *P*-favored phase (see the blue dash lines of R2). These results indicate that factors including atomic configuration, temperature, pressure, and S_{conf} make Al_5Fe_2 more stable. Figure 4 also shows that the $MoSi_2$-type Al_2Fe is *T*-unfavored, but it is a strong *P*-favored phase. In addition, the S_{conf} has less contribution to ΔG_{reac} in comparison with that for Al_5Fe_2, due to the less partially occupied Wyckoff site of Al_2Fe; see Eqs. (4) and (5). The *T*-unfavored behavior is caused by the lower phonon DOS of Al_2Fe than those of AlFe and $Al_{13}Fe_4$; see details in Supplementary Material. With increasing pressure, Fig. 4 shows that the ΔG_{reac} value of reaction R3 decreases greatly; for example, dropping more than 2 kJ/mol-atom at $T = 0$ K as well as at other temperatures. Experimentally, the $MoSi_2$-type Al_2Fe was synthesized through the laser-heated diamond-anvil cell at 10 GPa and 1873 K[95], and it was suggested that it is a high pressure phase existing at $P > 5$ GPa[68]; these experiments agree with the present conclusion that Al_2Fe is a *T*-unfavored but a strong *P*-favored phase, albeit it is stable at $T = 0$ K and $P = 0$ GPa (Fig. 3).

Figure 5 shows a schematic *P*–*T* phase diagram (demonstrated with $P = 0$ and 6 GPa) for the Al–Fe system based on the present DFT calculations using Eq. (3) based on the convex hull approach by considering all ΔG_{reac} values. As an example, the ΔG_{reac} values at $P = 0$ GPa for six reactions are shown in the Supplementary Figure S2, where the reaction R4 can be used to determine the critical temperatures of Al_5Fe_2 in some temperatures and pressures. Figure 5 indicates that $Al_{13}Fe_4$, AlFe, and $AlFe_3$ are always the stable IMCs marked by the shaded regions. However, at low pressures and low temperatures (e.g., $P = 0$ GPa and $T < 165$ K), the $L1_2$-type $AlFe_3$ is more stable than the $D0_3$-type $AlFe_3$. It is worth mentioning that $AlFe_3$ from DFT-based predictions is either a $L1_2$ structure or a $D0_3$ structure depended on the selected X-C functional[96,97]. The commonly used X-C functional of GGA predicts that the $L1_2$-$AlFe_3$ is more stable at 0 K with respect to the $D0_3$-$AlFe_3$ (see Table S1 as well as the results in the literature[63,96,97]). However, the energy difference between the $L1_2$ and $D0_3$ structures of $AlFe_3$ is very small (< 0.1 kJ/mol-atom, see Table S1), which is within the uncertainty of DFT predictions. Regardless of the stable structure at 0 K for $AlFe_3$ ($L1_2$ vs. $D0_3$), the present work shows that vibrational entropy makes the $D0_3$ structure more stable at high temperatures (> 165 K and $P = 0$ GPa) and/or at high pressures (> ~ 1 GPa); agreeing with the experimentally observed $AlFe_3$ with the $D0_3$ structure[9]. Over the entire temperature range in Fig. 5, Al_6Fe is not stable at $P = 0$ GPa, but is stable at higher pressures. Al_5Fe_2 (configuration predicted by USPEX) is stable at high temperatures (e.g., $T > 345$ K with $P = 0$ GPa), while higher pressures decrease its stability slightly. The $MoSi_2$-type Al_2Fe is a *T*-unfavored but a strong *P*-favored phase.

In comparison with the IMCs reported in the CALPHAD modelled Al–Fe phase diagram at $P = 0$ K and low temperatures (e.g., < 1000 K in Fig. 1), the DFT-based predictions in Fig. 5 agree reasonably well with those by the CALPHAD modeling, including the existed $Al_{13}Fe_4$, AlFe, and $AlFe_3$, as well as the absent Al_6Fe. The deviations are only for Al_5Fe_2 and Al_2Fe, which are stable at low temperatures (e.g., < 1000 K) by CALPHAD modeling but are not always stable by DFT-based predictions, indicating that the present configurations of Al_5Fe_2 and Al_2Fe are still not the lowest energy ones. It should be mentioned that the presently predicted Al_5Fe_2 configuration (see Table S2) has the lowest energy than the configurations reported in the literature (see Table S1)[67], while the presently predicted $MoSi_2$-type Al_2Fe is the same as the one suggested by Tobita et al.[68] To the best of our knowledge, the present configurations are the lowest energy ones which can be currently predicted for Al_5Fe_2 and Al_2Fe, but future efforts are still needed to predict new lower energy configurations by using larger supercells or new approaches.

Al–Fe IMCs[a]	Ductility	*P*-favored?	*T*-favored?
Al_6Fe	Ductile	Yes	Not, or less effect
$Al_{13}Fe_4$ (θ, Al_3Fe[9])	Slightly brittle	Always on convex hull[b]	Always on convex hull[b]
Al_5Fe_2 (η, Al_8Fe_3[98])	Brittle	Not, or less effect	Yes
Al_2Fe ($MoSi_2$-type)	Brittle	Yes, and strong	Not
Al_8Fe_5 ($D8_2$, ε[9])	Ductile	Less effect	Less effect
AlFe (B_2)	Slightly brittle	Always on convex hull[b]	Always on convex hull[b]
$AlFe_3$ ($D0_3$)	Ductile	Yes	Yes

Table 2. Summary of phase stability of key Al–Fe IMCs with respect to pressure (*P*) and temperature (*T*) shown in Figs. 1, 3, and 5 (or not shown); together with their ductility/brittleness according to Pugh's criterion[11,12] as shown in Fig. 2. [a]Names used in the present work together with the names in the parentheses used in the literature. [b]These IMCs are always stable and on the convex hull in the present *P* and *T* of studied.

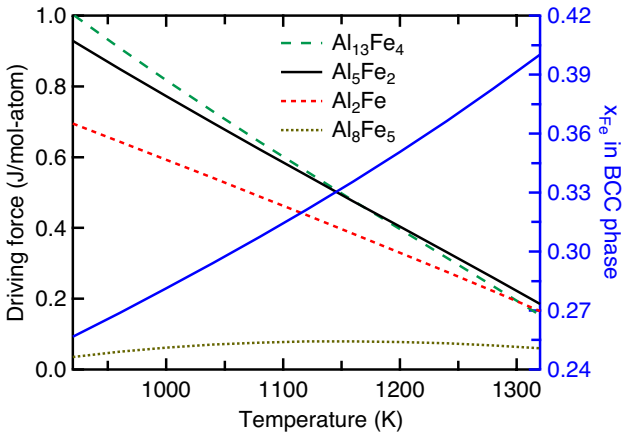

Figure 6. Thermodynamic driving forces of Al–Fe IMCs as a function of temperature (T = 920–1320 K) as well as the associated mole fraction of Fe (x_{Fe} = 0.26–0.40) along the metastable solidus line as shown in Fig. 1. Here, the Al–Fe thermodynamic properties were modelled by Sundman et al.[9].

Table 2 summarizes phase stability of Al–Fe IMCs as a function of pressure and temperature as shown in Figs. 1, 3, and 5; together with their ductility/brittleness judged by Pugh's criterion[11,12] as shown in Fig. 2, which were determined by the presently predicted elastic constants in Table S3.

Non-equilibrium Al–Fe IMCs by thermodynamic and kinetic analyses. In this section, we show first the formation of non-equilibrium IMCs by thermodynamic driving forces and kinetic analyses ("Non-equilibrium IMCs by thermodynamic driving forces and kinetic analyses" section); and then, we show the formation of non-equilibrium IMCs by Scheil simulations ("Non-equilibrium IMCs by Scheil simulations" section).

Non-equilibrium IMCs by thermodynamic driving forces and kinetic analyses. Figure 6 shows the predicted thermodynamic driving forces of the Al–Fe IMCs as a function of temperature (T = 920–1320 K) as well as the associated mole fraction of Fe (x_{Fe} = 0.28–0.40) along the metastable solidus line as shown in Fig. 1. Note that the eutectic reaction temperature is 927 K and the chosen thermodynamic description was that modelled by Sundman et al.[9]. It is seen that both $Al_{13}Fe_4$ and Al_5Fe_2 have the higher thermodynamic driving forces of formation at lower temperatures (< 1280 K) than those of Al_2Fe and Al_8Fe_5. By examining atomic diffusivity in Al–Fe IMCs, the interdiffusion coefficients in Al_5Fe_2 are at least two orders of magnitude faster than those in the other IMCs (AlFe, Al_2Fe, and $Al_{13}Fe_4$) at T = 823 – 913 K[42] and are comparable with the diffusion coefficients of dilute Fe in FCC Al; see Fig. 7 the diffusion coefficients reported in the literature[42,58,59]. In addition, Al atoms have higher diffusivity in Al_5Fe_2 than Fe atoms[38]. The fastest atomic diffusivity, especially Al atoms, in Al_5Fe_2 is due mainly to the rich Al vacancies in Al_5Fe_2[60]; see Eq. (1). However, considerable vacancies have not been reported in the other Al–Fe IMCs. By considering both the high thermodynamic driving force of formation (Fig. 6) and the fastest interdiffusion coefficients (Fig. 7), the brittle Al_5Fe_2 is the IMC with the largest possibility to be formed; see the Al-rich examples in Table 1, excepting those with extremely high Al contents, formed below the eutectic reaction temperature of 927 K, or processed by AM (examples #1 to #5, and #7 to #11).

Non-equilibrium IMCs by Scheil simulations. As two examples of fast cooling solidification, Fig. 8 shows the calculated mole fractions of solid phases by Scheil simulations using the thermodynamic description modelled

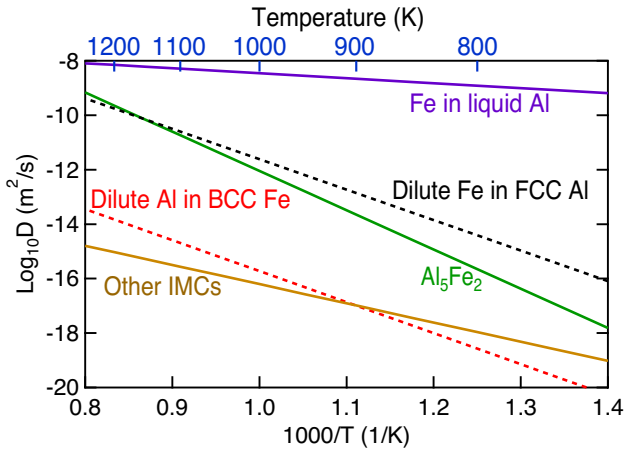

Figure 7. Diffusion coefficients of Fe in liquid Al[58], dilute Fe in FCC Al[58], dilute Al in BCC Fe[59], and the elements in Al_5Fe_2 and other IMCs (AlFe, Al_2Fe, and $Al_{13}Fe_4$)[42].

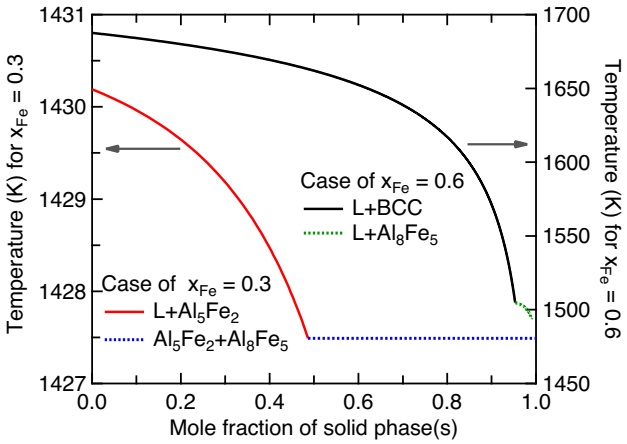

Figure 8. Calculated mole fractions of solid phases with $x_{Fe} = 0.3$ and 0.6 based on Scheil simulations using the thermodynamic description modelled by Sundman et al.[9].

by Sundman et al.[9]. With decreasing tempeature at the fixed composition of $x_{Fe} = 0.3$, the solid phase of Al_5Fe_2 forms first and reaches a maximum mole fracition about 0.5 at $T = 1427.5$ K, and then the second solid phase of Al_8Fe_5 forms at almost the fixed temperature of 1427.5 K. Due to the exteremely small temperture range ($<< 1$ K) for phase transition, Al_8Fe_5 was not observed in all the processes in Table 1. For the case of $x_{Fe} = 0.6$, the first solid phase formed with decreasing temperature is BCC (or the B2 phase), which reaches a maximum mole fraction of 0.95, and then Al_8Fe_5 forms in a small temperature range of 1505–1493 K. Similar to the case of $x_{Fe} = 0.3$, the predicted Al_8Fe_5 was also not observed in the processes in Table 1 due probably to the small temperature range of phase formation. Figure 9 shows the complete non-equilibrium phase diagram by Scheil simulations using the modelled Al–Fe system by Sundman et al.[9]. This non-equilibrium phase diagram shows the temperatures of the forming phases, though the lever rule cannot be used to determine phase fractions. Both the equilibrium phase diagram (Fig. 1) and the Scheil non-equilibrium phase diagram (Fig. 9) can be used to determine the forming phases in the slow/equilibrium and the fast cooling processes, respectively.

As an example to examine equilibrium and Scheil simulations, Fig. 10 show the forming phases as a function of temperature with $x_{Fe} = 0.4$. The forming phases are BCC and Al_8Fe_5 (majorly) based on Scheil simulations (see also Fig. 9), while the forming phases are Al_8Fe_5 (when $T > 1360$ K), BCC, and Al_2Fe based on equilibrium calculations (see also Fig. 1). Therefore, the forming phases could be BCC, Al_2Fe, and/or Al_8Fe_5 depended on different processes. For instance, Stein et al.[99] observed the eutectoid reaction of $Al_8Fe_5 \leftrightarrow Al_2Fe + BCC$ (B2) at 1368 K by the differential thermal analyses for the Al-40 at.% Fe alloy ($x_{Fe} = 0.4$) at the heating rates of 5 and 10 K/min.

It should be remarked that the forming phases depend mainly on compositions (especially the local compositions) in addition to temperature, pressure, and atomic diffusivity for the system of interest. Table 1 shows that AM is superior to the other processes in achieving desired phases such as AlFe and $AlFe_3$ through varying the compositions. To predict the forming IMCs under a given composition and a given processing history, the combined thermodynamic and kinetic simulations are needed. For example, Lindwall et al.[100] simulated the

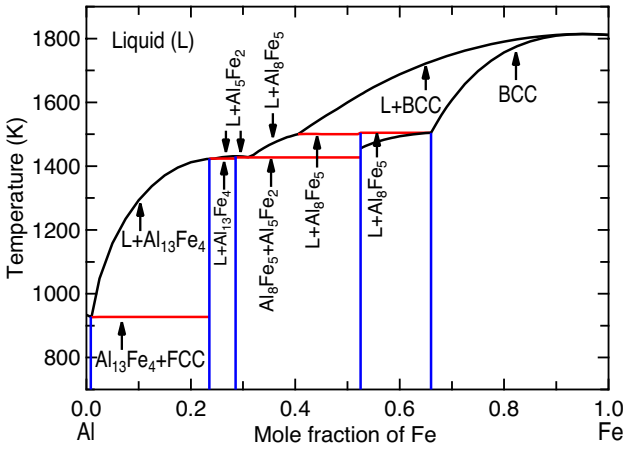

Figure 9. Predicted Al–Fe non-equilibrium phase diagram by Scheil simulations uisng the modelled data by Sundman et al.[9], showing the forming temperatures for the phases indicated by the lines. Note that the lever rule cannot be used to determine phase fractions (see Fig. 8 for two examples).

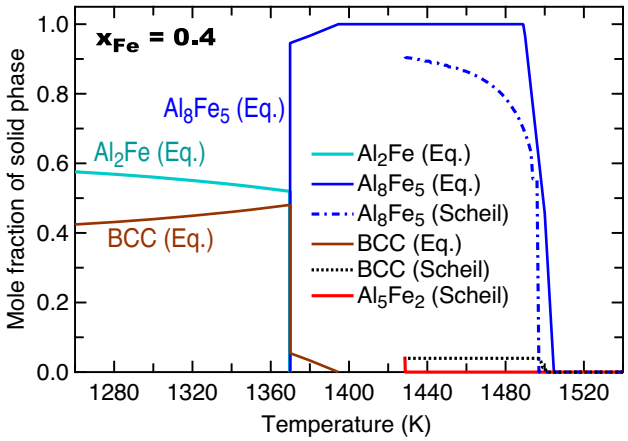

Figure 10. Calculated mole fracitons of solid phases with $x_{Fe} = 0.4$ based on Scheil simulations and equilibrium (Eq.) calculations using the modelled data by Sundman et al.[9].

time–temperature-transformation (TTT) diagram and the forming IMCs in the additively manufactured Ni-based Inconel 625. However, these simulations are beyond the scope of the present work.

Summary

The present work investigated the forming mechanism of equilibrium and non-equilibrium intermetallic compounds (IMCs) in dissimilar aluminum/steel (Al–Fe) joints by means of Gibbs energy as a function of temperature (T) and pressure (P) from (i) first-principles phonon calculations, (ii) equilibrium Al–Fe phase diagram in the literature and the presently predicted non-equilibrium phase diagram by Scheil simulations, (iii) atomic diffusivity in Al–Fe, and (iv) experimentally observed IMCs in various processes (*cf.*, Table 1). In particular, the unknown atomic configurations of Al_2Fe and Al_5Fe_2 were examined in the present work by machine learning based datamining together with first-principles verifications and structure predictor (using USPEX). To the best of our knowledge, the presently predicted configurations of Al_2Fe and Al_5Fe_2 possess lower energies in comparison with the configurations reported in the literature. However, the present configurations are still not the lowest energy ones, hence appealing for future efforts. In addition, the predicted $MoSi_2$-type Al_2Fe is a pressure-favored IMC, instead of the phase with space group $P\bar{1}$ shown in the experimental phase diagram. Note that the present DFT-based thermodynamics is based on the quasiharmonic approach with the possible sources of error from such as the ignorance of anharmonicity, the adoption of ideal configurational entropy, the unknown atomic configurations of Al_5Fe_2 and Al_2Fe, and the approximations adopted in density functional theory.

Al–Fe IMCs formed in various experimental processes are summarized in Table 1 ("Introduction" section). The present work concludes that the formation of IMCs can be explained well by phase diagrams, thermodynamic driving forces, P- and T-included Gibbs energy, and atomic diffusion coefficients. Specifically, the metastable and ductile Al_6Fe is a P-favored IMC, which was observed in Al-dominant samples and the processes involving

pressures such as direct-chill casting, die casting, equal channel angular extrusion. Here the ductility and brittleness of IMCs were judged by Pugh's criterion[11,12] using the presently predicted elastic constants. The $MoSi_2$-type Al_2Fe is a brittle and strong *P*-favored IMC observed at high pressures. The stable but brittle η-Al_5Fe_2 is the most observed IMC usually adjacent to steel (Fe) in almost all the processes as detailed in Table 1, such as fusion or solid-state welding, immersion testing, diffusion couples, and additive manufacturing (AM), since Al_5Fe_2 is a *T*-favored phase with a high thermodynamic driving force of formation and the fastest atomic diffusivity among all Al–Fe IMCs. The slightly brittle θ-$Al_{13}Fe_4$ is the second most observed IMC usually adjacent to Al shown in most of the processes, possessing the highest thermodynamic driving force of formation in Al-rich side. Notably, the ductile $AlFe_3$, the less ductile AlFe, and almost all the other IMCs were observed in the AM processes, making AM an exceptional way to tailor composition and in turn achieve the desired IMCs in dissimilar materials. All the IMCs (without the *P*-favored phases) formed in the Al–Fe joints can be identified using the equilibrium and the Scheil non-equilibrium phase diagrams, together with kinetic considerations.

Received: 23 July 2021; Accepted: 29 November 2021
Published online: 20 December 2021

References

1. Wang, P., Chen, X., Pan, Q., Madigan, B. & Long, J. Laser welding dissimilar materials of aluminum to steel: an overview. *Int. J. Adv. Manuf. Technol.* **87**, 3081–3090 (2016).
2. Sakundarini, N., Taha, Z., Abdul-Rashid, S. H. & Ghazila, R. A. R. Optimal multi-material selection for lightweight design of automotive body assembly incorporating recyclability. *Mater. Des.* **50**, 846–857 (2013).
3. Wargnier, H., Kromm, F. X., Danis, M. & Brechet, Y. Proposal for a multi-material design procedure. *Mater. Des.* **56**, 44–49 (2014).
4. Bahraminasab, M. *et al.* Multi-objective design optimization of functionally graded material for the femoral component of a total knee replacement. *Mater. Des.* **53**, 159–173 (2014).
5. Aizawa, T., Okagawa, K. & Kashani, M. Application of magnetic pulse welding technique for flexible printed circuit boards (FPCB) lap joints. *J. Mater. Process. Technol.* **213**, 1095–1102 (2013).
6. Springer, H., Kostka, A., dos Santos, J. F. & Raabe, D. Influence of intermetallic phases and Kirkendall-porosity on the mechanical properties of joints between steel and aluminium alloys. *Mater. Sci. Eng. A* **528**, 4630–4642 (2011).
7. Safeen, M. W. & Russo Spena, P. Main issues in quality of friction stir welding joints of aluminum alloy and steel sheets. *Metals (Basel)* **9**, 610 (2019).
8. Hussein, S. A., Tahir, A. S. M. & Hadzley, A. B. Characteristics of aluminum-to-steel joint made by friction stir welding: A review. *Mater. Today Commun.* **5**, 32–49 (2015).
9. Sundman, B., Ohnuma, I., Dupin, N., Kattner, U. R. & Fries, S. G. An assessment of the entire Al–Fe system including $D0_3$ ordering. *Acta Mater.* **57**, 2896–2908 (2009).
10. Aliravci, C. A. & Pekgüleryüz, M. Ö. Calculation of phase diagrams for the metastable Al-Fe phases forming in direct-chill (DC)-cast aluminum alloy ingots. *Calphad* **22**, 147–155 (1998).
11. Pugh, S. F. X. C. I. I. Relations between the elastic moduli and the plastic properties of polycrystalline pure metals. *Philos. Mag.* **45**, 823–843 (1954).
12. Liu, Z. Q. *et al.* Electrically reversible cracks in an intermetallic film controlled by an electric field. *Nat. Commun.* **9**, 41 (2018).
13. Zhu, X., Blake, P. & Ji, S. The formation mechanism of Al_6(Fe, Mn) in die-cast Al-Mg alloys. *CrystEngComm* **20**, 3839–3848 (2018).
14. Yu, F., Liu, F., Zhao, D. & Toth, L. S. Microstructure and mechanical properties of Al-3Fe alloy processed by equal channel angular extrusion. In *IOP Conference Series: Materials Science and Engineering* Vol. 63, 012079 (2014).
15. He, H., Lin, S., Yang, C., Fan, C. & Chen, Z. Combination effects of nocolok flux with ni powder on properties and microstructures of aluminum-stainless steel TIG welding-brazing joint. *J. Mater. Eng. Perform.* **22**, 3315–3323 (2013).
16. Qi, X., Takata, N., Suzuki, A., Kobashi, M. & Kato, M. Laser powder bed fusion of a near-eutectic Al–Fe binary alloy: Processing and microstructure. *Addit. Manuf.* **35**, 101308 (2020).
17. Shishkovsky, I., Missemer, F., Kakovkina, N. & Smurov, I. Intermetallics synthesis in the Fe–Al system via layer by layer 3D laser cladding. *Curr. Comput.-Aided Drug Des.* **3**, 517–529 (2013).
18. Pęska, M., Karczewski, K., Rzeszotarska, M. & Polański, M. Direct synthesis of Fe–Al alloys from elemental powders using laser engineered net shaping. *Materials (Basel).* **13**, 531 (2020).
19. Lotfian, S., Rolink, G., Weisheit, A. & Palm, M. Chemically graded Fe-Al/steel samples fabricated by laser metal deposition. *MRS Adv.* **2**, 1393–1398 (2017).
20. Shen, C., Pan, Z., Cuiuri, D., Roberts, J. & Li, H. Fabrication of Fe-FeAl Functionally Graded Material Using the Wire-Arc Additive Manufacturing Process. *Metall. Mater. Trans. B* **47**, 763–772 (2016).
21. Shen, C., Pan, Z., Ma, Y., Cuiuri, D. & Li, H. Fabrication of iron-rich Fe-Al intermetallics using the wire-arc additive manufacturing process. *Addit. Manuf.* **7**, 20–26 (2015).
22. Yamagiwa, K., Watanabe, Y., Fukui, Y. & Kapranos, P. Novel recycling system of aluminum and iron wastes-in-situ Al-Al_3Fe functionally graded material manufactured by a centrifugal method. *Mater. Trans.* **44**, 2461–2467 (2003).
23. Kemerling, B., Lippold, J. C., Fancher, C. M. & Bunn, J. Residual stress evaluation of components produced via direct metal laser sintering. *Weld. World* **62**, 663–674 (2018).
24. Wu, A. S., Brown, D. W., Kumar, M., Gallegos, G. F. & King, W. E. An experimental investigation into additive manufacturing-induced residual stresses in 316L stainless steel. *Metall. Mater. Trans. A* **45**, 6260–6270 (2014).
25. Fan, J., Thomy, C. & Vollertsen, F. Effect of thermal cycle on the formation of intermetallic compounds in laser welding of aluminum-steel overlap joints. *Phys. Procedia* **12**, 134–141 (2011).
26. Wang, C. *et al.* The influence of heat input on microstructure and mechanical properties for dissimilar welding of galvanized steel to 6061 aluminum alloy in a zero-gap lap joint configuration. *J. Alloys Compd.* **726**, 556–566 (2017).
27. Meco, S., Ganguly, S., Williams, S. & McPherson, N. Effect of laser processing parameters on the formation of intermetallic compounds in Fe-Al dissimilar welding. *J. Mater. Eng. Perform.* **23**, 3361–3370 (2014).
28. Elrefaey, A., Gouda, M., Takahashi, M. & Ikeuchi, K. Characterization of aluminum/steel lap joint by friction stir welding. *J. Mater. Eng. Perform.* **14**, 10–17 (2005).
29. Abbasi, M., Dehghani, M., Guim, H. U. & Kim, D. I. Investigation of Fe-rich fragments in aluminum-steel friction stir welds via simultaneous transmission Kikuchi diffraction and EDS. *Acta Mater.* **117**, 262–269 (2016).
30. Das, H., Ghosh, R. N. & Pal, T. K. Study on the formation and characterization of the intermetallics in friction stir welding of aluminum alloy to coated steel sheet lap joint. *Metall. Mater. Trans. A* **45**, 5098–5106 (2014).

31. Haghshenas, M. *et al.* Friction stir weld assisted diffusion bonding of 5754 aluminum alloy to coated high strength steels. *Mater. Des.* **55**, 442–449 (2014).
32. Movahedi, M. *et al.* Growth kinetics of Al-Fe intermetallic compounds during annealing treatment of friction stir lap welds. *Mater. Charact.* **90**, 121–126 (2014).
33. Taban, E., Gould, J. E. & Lippold, J. C. Dissimilar friction welding of 6061–T6 aluminum and AISI 1018 steel: Properties and microstructural characterization. *Mater. Des.* **31**, 2305–2311 (2010).
34. Bozzi, S., Helbert-Etter, A. L., Baudin, T., Criqui, B. & Kerbiguet, J. G. Intermetallic compounds in Al 6016/IF-steel friction stir spot welds. *Mater. Sci. Eng. A* **527**, 4505–4509 (2010).
35. Wang, K. *et al.* Investigation of interfacial layer for friction stir scribe welded aluminum to steel joints. *J. Manuf. Sci. Eng.* **140**, 111005 (2018).
36. Najafi, A., Movahedi, M. & Yarandi, A. S. Properties–microstructure relationship in Al–Fe in situ composite produced by friction stir processing. *Proc. Ins. Mech. Eng. Part L J. Mater. Des. Appl.* **233**, 1955–1965 (2019).
37. Agudo, L. *et al.* Intermetallic Fe_xAl_y-phases in a steel/Al-alloy fusion weld. *J. Mater. Sci.* **42**, 4205–4214 (2007).
38. Zhang, G., Chen, M., Shi, Y., Huang, J. & Yang, F. Analysis and modeling of the growth of intermetallic compounds in aluminum-steel joints. *RSC Adv.* **7**, 37797–37805 (2017).
39. Ding, Z. *et al.* Microstructural evolution and growth behavior of intermetallic compounds at the liquid Al/solid Fe interface by synchrotron X-ray radiography. *Mater. Charact.* **136**, 157–164 (2018).
40. Bouché, K., Barbier, F. & Coulet, A. Intermetallic compound layer growth between solid iron and molten aluminium. *Mater. Sci. Eng. A* **249**, 167–175 (1998).
41. Bouayad, A., Gerometta, C., Belkebir, A. & Ambari, A. Kinetic interactions between solid iron and molten aluminium. *Mater. Sci. Eng. A* **363**, 53–61 (2003).
42. Naoi, D. & Kajihara, M. Growth behavior of Fe_2Al_5 during reactive diffusion between Fe and Al at solid-state temperatures. *Mater. Sci. Eng. A* **459**, 375–382 (2007).
43. Tanaka, Y. & Kajihara, M. Kinetics of isothermal reactive diffusion between solid Fe and liquid Al. *J. Mater. Sci.* **45**, 5676–5684 (2010).
44. Wang, X., Wood, J. V., Sui, Y. & Lu, H. Formation of intermetallic compound in iron-aluminum alloys. *J. Shanghai Univ. (English Ed.)* **2**, 305–310 (1998).
45. Novák, P. *et al.* On the formation of intermetallics in Fe-Al system - An in situ XRD study. *Intermetallics* **32**, 127–136 (2013).
46. Van Alboom, A. *et al.* Multi-method identification and characterization of the intermetallic surface layers of hot-dip Al-coated steel: $FeAl_3$ or Fe_4Al_{13} and Fe_2Al_5 or Fe_2Al_{5+x}. *Surf. Coatings Technol.* **324**, 419–428 (2017).
47. Liu, Z.-K. Computational thermodynamics and its applications. *Acta Mater.* **200**, 745–792 (2020).
48. Schmid-Fetzer, R. Phase diagrams: the beginning of wisdom. *J. Phase Equilibria Diffus.* **35**, 735–760 (2014).
49. Scheil, E. Bemerkungen zur schichtkristallbildung. *Zeitschrift für Met.* **34**, 70–72 (1942).
50. Gulliver, G. H. The quantitative effect of rapid cooling upon the constitution of binary alloys. *J. Inst. Met* **9**, 120–157 (1913).
51. Moustafa, A. R., Durga, A., Lindwall, G. & Cordero, Z. C. Scheil ternary projection (STeP) diagrams for designing additively manufactured functionally graded metals. *Addit. Manuf.* **32**, 101008 (2020).
52. Bocklund, B., Bobbio, L. D., Otis, R. A., Beese, A. M. & Liu, Z.-K. Experimental validation of Scheil-Gulliver simulations for gradient path planning in additively manufactured functionally graded materials. *Materialia* **11**, 100689 (2020).
53. Schaffnit, P., Stallybrass, C., Konrad, J., Stein, F. & Weinberg, M. A Scheil-Gulliver model dedicated to the solidification of steel. *Calphad* **48**, 184–188 (2015).
54. Lee, H. M., Yoon, S. W. & Lee, B.-J. Thermodynamic prediction of interface phases at Cu/solder joints. *J. Electron. Mater.* **27**, 1161–1166 (1998).
55. Zhou, S. H. & Napolitano, R. E. Energetics of nonequilibrium solidification in Al-Sm. *Phys. Rev. B* **78**, 184111 (2008).
56. Wang, K. *et al.* Unveiling non-equilibrium metallurgical phases in dissimilar Al-Cu joints processed by vaporizing foil actuator welding. *Mater. Des.* **186**, 108306 (2020).
57. Andersson, J.-O., Helander, T., Höglund, L., Shi, P. & Sundman, B. Thermo-Calc & DICTRA: Computational tools for materials science. *Calphad* **26**, 273–312 (2002).
58. Du, Y. *et al.* Diffusion coefficients of some solutes in fcc and liquid Al: critical evaluation and correlation. *Mater. Sci. Eng. A* **363**, 140–151 (2003).
59. Helander, T. & Ågren, J. A phenomenological treatment of diffusion in Al–Fe and Al–Ni alloys having B2-b.c.c. ordered structure. *Acta Mater.* **47**, 1141–1152 (1999).
60. Burkhardt, U., Grin, Y., Ellner, M. & Peters, K. Structure refinement of the iron–aluminium phase with the approximate composition Fe_2Al_5. *Acta Crystallogr. Sect. B* **50**, 313–316 (1994).
61. Chumak, I., Richter, K. W. & Ehrenberg, H. Redetermination of iron dialuminide, $FeAl_2$. *Acta Crystallogr. Sect. C* **66**, i87–i88 (2010).
62. Lyakhov, A. O., Oganov, A. R., Stokes, H. T. & Zhu, Q. New developments in evolutionary structure prediction algorithm USPEX. *Comput. Phys. Commun.* **184**, 1172–1182 (2013).
63. Jain, A. *et al.* Commentary: The Materials Project: A materials genome approach to accelerating materials innovation. *APL Mater.* **1**, 011002 (2013).
64. Kirklin, S. *et al.* The Open Quantum Materials Database (OQMD): Assessing the accuracy of DFT formation energies. *npj Comput. Mater.* **1**, 15010 (2015).
65. van de Walle, A. *et al.* Efficient stochastic generation of special quasirandom structures. *Calphad* **42**, 13–18 (2013).
66. Glass, C. W., Oganov, A. R. & Hansen, N. USPEX - Evolutionary crystal structure prediction. *Comput. Phys. Commun.* **175**, 713–720 (2006).
67. Vinokur, A. I., Hilleke, K. P. & Fredrickson, D. C. Principles of weakly ordered domains in intermetallics: the cooperative effects of atomic packing and electronics in Fe_2Al_5. *Acta Crystallogr. Sect. A* **75**, 297–306 (2019).
68. Tobita, K. *et al.* Phase stability and thermoelectric properties of semiconductor-like tetragonal $FeAl_2$. *Sci. Technol. Adv. Mater.* **20**, 937–948 (2019).
69. Gražulis, S. *et al.* Crystallography Open Database – An open-access collection of crystal structures. *J. Appl. Crystallogr.* **42**, 726–729 (2009).
70. Gražulis, S. *et al.* Crystallography Open Database (COD): An open-access collection of crystal structures and platform for world-wide collaboration. *Nucleic Acids Res.* **40**, D420–D427 (2012).
71. Choudhary, K. *et al.* The joint automated repository for various integrated simulations (JARVIS) for data-driven materials design. *npj Comput. Mater.* **6**, 173 (2020).
72. Krajewski, A. M., Siegel, J. W., Xu, J. & Liu, Z.-K. Extensible Structure-informed prediction of formation energy with improved accuracy and usability employing neural networks. *arXiv*: 2008.13654 (2020).
73. Shang, S.-L., Wang, Y., Kim, D. & Liu, Z.-K. First-principles thermodynamics from phonon and Debye model: Application to Ni and Ni_3Al. *Comput. Mater. Sci.* **47**, 1040–1048 (2010).
74. Wang, A. *et al.* Effects of pressure and vibration on the thermal decomposition of cubic $Ti_{1-x}Al_xN$, $Ti_{1-x}Zr_xN$, and $Zr_{1-x}Al_xN$ coatings: A first-principles study. *J. Mater. Sci.* **47**, 7621–7627 (2012).

75. Wang, Y., Liu, Z. K. & Chen, L. Q. Thermodynamic properties of Al, Ni, NiAl, and Ni_3Al from first-principles calculations. *Acta Mater.* **52**, 2665–2671 (2004).
76. Glensk, A., Grabowski, B., Hickel, T. & Neugebauer, J. Understanding anharmonicity in fcc materials: from its origin to ab initio strategies beyond the quasiharmonic approximation. *Phys. Rev. Lett.* **114**, 195901 (2015).
77. de Wijs, G. A., Kresse, G. & Gillan, M. J. First-order phase transitions by first-principles free-energy calculations: the melting of Al. *Phys. Rev. B* **57**, 8223–8234 (1998).
78. Shang, S.-L., Wang, Y. & Liu, Z.-K. Thermodynamic fluctuations between magnetic states from first-principles phonon calculations: The case of bcc Fe. *Phys. Rev. B* **82**, 014425 (2010).
79. Liu, Z.-K., Wang, Y. & Shang, S. Thermal expansion anomaly regulated by entropy. *Sci. Rep.* **4**, 7043 (2015).
80. Shang, S.-L., Wang, Y., Anderson, T. J. & Liu, Z.-K. Achieving accurate energetics beyond (semi-)local density functional theory: Illustrated with transition metal disulfides, Cu_2ZnSnS_4, and Na_3PS_4 related semiconductors. *Phys. Rev. Mater.* **3**, 015401 (2019).
81. Kresse, G. & Furthmüller, J. Efficient iterative schemes for ab initio total-energy calculations using a plane-wave basis set. *Phys. Rev. B* **54**, 11169–11186 (1996).
82. Kresse, G. & Joubert, D. From ultrasoft pseudopotentials to the projector augmented-wave method. *Phys. Rev. B* **59**, 1758–1775 (1999).
83. Perdew, J. P., Burke, K. & Ernzerhof, M. Generalized gradient approximation made simple. *Phys. Rev. Lett.* **77**, 3865–3868 (1996).
84. Methfessel, M. & Paxton, A. T. High-precision sampling for Brillouin-zone integration in metals. *Phys. Rev. B* **40**, 3616–3621 (1989).
85. Blöchl, P. E., Jepsen, O. & Andersen, O. K. Improved tetrahedron method for Brillouin-zone integrations. *Phys. Rev. B* **49**, 16223–16233 (1994).
86. Wang, Y. *et al.* A mixed-space approach to first-principles calculations of phonon frequencies for polar materials. *J. Phys. Condens. Matter* **22**, 202201 (2010).
87. Wang, Y., Shang, S.-L., Fang, H., Liu, Z.-K. & Chen, L.-Q. First-principles calculations of lattice dynamics and thermal properties of polar solids. *npj Comput. Mater.* **2**, 16006 (2016).
88. Shang, S., Wang, Y. & Liu, Z.-K. First-principles elastic constants of α- and θ-Al_2O_3. *Appl. Phys. Lett.* **90**, 101909 (2007).
89. Shang, S. L. *et al.* First-principles calculations of pure elements: Equations of state and elastic stiffness constants. *Comput. Mater. Sci.* **48**, 813–826 (2010).
90. Hill, R. The elastic behaviour of a crystalline aggregate. *Proc. Phys. Soc. Sect. A* **65**, 349–354 (1952).
91. Simmons, G. & Wang, H. *Single crystal elastic constants and calculated aggregate properties: A handbook* (Press, 1971).
92. Ranganathan, S. I. & Ostoja-Starzewski, M. Universal elastic anisotropy index. *Phys. Rev. Lett.* **101**, 055504 (2008).
93. Hillert, M. *Phase equilibria, phase diagrams and phase transformations: Their thermodynamic basis* (Cambridge University Press, Cambridge, 2008).
94. Otis, R. & Liu, Z.-K. pycalphad: CALPHAD-based computational thermodynamics in Python. *J. Open Res. Softw.* **5**, 1 (2017).
95. Tobita, K. *et al.* High-pressure synthesis of tetragonal iron aluminide $FeAl_2$. *Scr. Mater.* **141**, 107–110 (2017).
96. Lechermann, F. *et al.* Density-functional study of Fe_3Al: LSDA versus GGA. *Phys. Rev. B* **65**, 132104 (2002).
97. Lechermann, F., Fähnle, M., Meyer, B. & Elsässer, C. Electronic correlations, magnetism, and structure of Fe-Al subsystems: An LDA study. *Phys. Rev. B* **69**, 165116 (2004).
98. Okamoto, N. L., Okumura, J., Higashi, M. & Inui, H. Crystal structure of η'-Fe_3Al_8; low-temperature phase of η-Fe_2Al_5 accompanied by an ordered arrangement of Al atoms of full occupancy in the c-axis chain sites. *Acta Mater.* **129**, 290–299 (2017).
99. Stein, F., Vogel, S. C., Eumann, M. & Palm, M. Determination of the crystal structure of the ε phase in the Fe-Al system by high-temperature neutron diffraction. *Intermetallics* **18**, 150–156 (2010).
100. Lindwall, G. *et al.* Simulation of TTT curves for additively manufactured Inconel 625. *Metall. Mater. Trans. A* **50**, 457–467 (2019).

Acknowledgements

The authors acknowledge the financial support partially by the U.S. Department of Energy (DOE) via Award No. DE-EE0008456; and partially by the National Science Foundation (NSF) with Grant No. CMMI-1825538. The authors thank John Shimanek for reading the manuscript. First-principles calculations were performed partially on the Roar supercomputer at the Pennsylvania State University's Institute for Computational and Data Sciences (ICDS), partially on the resources of the National Energy Research Scientific Computing Center (NERSC) supported by the U.S. DOE Office of Science User Facility operated under Contract No. DE-AC02-05CH11231, and partially on the resources of the Extreme Science and Engineering Discovery Environment (XSEDE) supported by NSF with Grant No. ACI-1548562.

Author contributions

S.L.S. performed DFT calculations and wrote the main manuscript; H.S. performed the Scheil simulations; B.P. analyzed the Al-Fe dissimilar joints; Y.W. performed DFT calculations; A.M.K. performed ML simulations; M.B., J.J.L., and Z.K.L. supervised this work. All authors reviewed the manuscript.

Competing interests

The authors declare no competing interests.

Additional information

Supplementary Information The online version contains supplementary material available at https://doi.org/10.1038/s41598-021-03578-0.

Correspondence and requests for materials should be addressed to S.-L.S.

Reprints and permissions information is available at www.nature.com/reprints.

Publisher's note Springer Nature remains neutral with regard to jurisdictional claims in published maps and institutional affiliations.